Hindawi
International Journal of Photoenergy
Volume 2022, Article ID 6412430, 13 pages
https://doi.org/10.1155/2022/6412430

*Research Article*

# Simulation Study to Predict Generation Power of a Vehicle Photovoltaic System

**Shiwu Li**,[1] **Minghao Fu**,[1] **Xueda Li**,[1] **Mengzhu Guo**,[1,2] **Mingyang Li**,[1] **Xueping Yao**,[3] **and Bingkui Ji**[3]

[1]*Transportation College of Jilin University, Changchun, China*
[2]*State Key Laboratory of Automotive Simulation and Control, Jilin University, Changchun, China*
[3]*Changchun Institute of Technology, Changchun, China*

Correspondence should be addressed to Mengzhu Guo; guomz@jlu.edu.cn

Received 29 September 2021; Revised 3 March 2022; Accepted 12 April 2022; Published 24 May 2022

Academic Editor: Pierluigi Guerriero



The integration of solar photovoltaic (PV) power generation technology into electric vehicle (EV) charging systems is of great significance, and it is very important to analyze the influencing factors of vehicle operating parameters on the generation power of vehicle PV system. In this paper, a model is developed to predict the power generated by vehicle PV system through a combination of a Fluent simulation study and Simulink modeling. Then the generation power of vehicle PV system under 7 different vehicle speeds in different months in Northeast China is analyzed. Through the Spearman correlation analysis and multilevel function fitting of the data, the mathematical model of a vehicle PV system power is proposed. Its variation with vehicle speed is obtained, as affected by solar radiation intensity and ambient temperature. According to the mathematical model analysis, the relevant vehicle characteristics and rules for vehicle PV systems were obtained. The simulation results show that the generation power of vehicle PV system in Northeast China increases significantly with the increase of vehicle speed in summer, but does not change significantly with the increase of vehicle speed in winter.

## 1. Introduction

With the growing popularity of electric vehicles, the issue of improving their battery capacity and range has been studied by the many scholars [1, 2]. Due to the fact that the capacity of electric vehicles' lithium batteries is difficult to greatly expand, on-vehicle photovoltaic battery charging has become another method to improve the range of electric vehicles [3]. As an auxiliary power source for electric vehicles, photovoltaic cells have broad research prospects because they do not use fossil fuels, which helps with environmental protection and convenient energy acquisition [4, 5].

The output power of photovoltaic cells is mainly affected by the incident solar radiation intensity and the photovoltaic cells' surface temperatures. The surface temperatures of photovoltaic cells are due to the ambient temperature and the surface temperature rise over ambient ($\Delta T$) of photovoltaic cells. Many scholars have proposed a variety of models to predict the output power of photovoltaic cells according to these influencing factors. Abo-Zahhad et al. analyzed the performance, limits, and thermal stresses seen by highly polycrystalline photovoltaic cells under highly concentrated sunlight and passive cooling conditions and proposed a comprehensive three-dimensional coupled thermal structure model [6]. The three-dimensional coupled thermal model of perovskite photovoltaic cells can effectively analyze the heat flux density they see, and the heat dissipation characteristics and other factors influencing them, to improve their power generation efficiency [7, 8]. Dabaghzadeh and Eslami developed a computational fluid dynamics (CFD) model to study photovoltaic temperatures and simulate the three-dimensional airflow field around a system under different geometric and environmental conditions and predict the temperature distribution and output power of the photovoltaic module [9]. The CFD simulation study of the three-dimensional flow fields around the photovoltaic cell is also

suitable for studying the power generation efficiency of low solar radiation conditions and the influence of surface contamination on photovoltaic cells' power [10–12]. Perovic et al. proposed a thermal model to model the temperature of photovoltaic cells according to the meteorological conditions, the locations of the photovoltaic cells, and their technical characteristics and determined their power and efficiency with consideration of their predicted temperatures [13]. Zhiqiang and Dongyang proposed a neural network-based photovoltaic power prediction model based on the Hilbert transform and frequency entropy to solve the problem that the power fluctuations from photovoltaic power stations affect the dispatch operations and stability of the power grid incorporating substantial percentages of photovoltaic power [14]. Yadir et al. proposed a method to extract the physical parameters for the single diode model of photovoltaic cells, to estimate the temperature coefficients for current and voltage at the maximum power point, and to predict the performance of photovoltaic cells for varied conditions [15]. Kasburg and Frizzo proposed a long-term memory method (LSTM) as a deep learning artificial recurrent neural network structure to predict the output power of photovoltaic cells [16]. Asef et al. verified IEC61853 based on empirical research. They improved the output power predictions for photovoltaic modules, taking into account the nominal working cell temperatures [17]. S. Issaadi et al. proposed a photovoltaic control strategy based on neural networks which smoothens the signals in power systems with PV sources and improves predictions' accuracy [18]. Jatoi et al. developed an empirical model to predict the effects of temperature on different photovoltaic modules' performance in outdoor environments and verified the model with experiments [19]. Due to the variability of meteorological conditions, a temperature-based predictive model needs to consider the influence of temperature variations resulting from different meteorological conditions [20, 21]. Zang et al. proposed and verified a new day-ahead photovoltaic power prediction method based on a deep learning neural network and verified their method with an example [22]. Tripathy et al. aimed at the randomness of weather conditions, proposing an averaging model for probabilistic PV generation forecasting based on K-nearest neighbor, which is verified by the real photovoltaic power generation data from the USA [23]. Ranjan et al. proposed an improved sliding window prediction (ISWP) which can be used for the preprocessing of fluctuating time series such as wind power generation and solar radiation [24]. Bhat et al. applied the extended cumulant method (ECM) to the probabilistic load flow (PLF) assessment in transmission and distribution systems, and the uncertainty of PV power generation is modeled by probability [25].

To sum up, for photovoltaic cell output power prediction models, some scholars have estimated the solar radiation intensity and temperature for different conditions, and then predict PV arrays' output power. However, for a vehicle photovoltaic system, there are relatively few studies on the influence of photovoltaic cells on the running process of electric vehicles. Therefore, the main contributions of the research are as follows:

(1) In this paper, a semiflexible photovoltaic cell was installed on the surface of an electric vehicle, and the temperature field of the photovoltaic cell on the vehicle surface was simulated and analyzed for the specific meteorological conditions. These data were combined with a mathematical model for the photovoltaic cell

(2) This model can predict the output power of the photovoltaic cells for variable conditions of solar radiation, ambient temperature, and vehicle speed

(3) The comprehensive effects of vehicle speed, solar radiation, and ambient temperatures on the vehicle photovoltaic system are analyzed

This paper contains five parts. The second part mainly introduces the working principle of the vehicle-mounted photovoltaic cell and the establishment of its mathematical model. The third part mainly introduces the simulation process. The fourth part analyzes the simulation results. Finally, the fifth part summarizes the results.

## 2. Developing the Mathematical Model

*2.1. Photovoltaic Cell Model.* According to the principles of photovoltaic cells, the main parts of photovoltaic cells include PN diode junction structures: and photovoltaic cells can be regarded as a parallel structure of a constant current source and this PN junction. Figure 1 shows the equivalent circuit of a photovoltaic cell, where $C_j$ and $C_d$ are barrier capacitance and diffusion capacitance at the junction, and $R_s$ and $R_{sh}$ are the series and parallel resistances inside the cell.

Because the response rate of power system loads is very slow compared with the time constant of most photovoltaic cells, the influence of junction capacitance can be ignored and the I-U characteristic equation can be obtained from the equivalent circuit [26].

$$I = I_L - I_0\left\{\exp\left[\frac{q(U+IR_s)}{AKT}\right]-1\right\}-\frac{U+IR_s}{R_{sh}}. \quad (1)$$

In Equation (1), $I_0$ is the reverse saturation current (A), $q$ is the electronic charge ($1.6\times10^{-19}C$), $K$ is the Boltzmann constant ($1.38\times10^{-23}$J/K), $T$ is the absolute temperature (K), A is the diode factor, $I_L$ is the photocurrent (A), $I$ is the output current of the PV cell (A), and $U$ is the output voltage of the PV cell (V).

For more convenience in the mathematical model building and analysis, Equation (1) is simplified, and the following reduced models are obtained:

$$I = I_{SC}\left\{1-C_1\left[\exp\left(\frac{U}{C_2U_{OC}}\right)-1\right]\right\}, \quad (2)$$

$$C_1 = \left(1-\frac{I_m}{I_{SC}}\right)\exp\left(\frac{U_m}{C_2U_{OC}}\right), \quad (3)$$

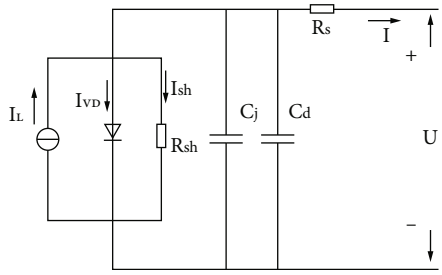


Figure 1: Equivalent circuit of a photovoltaic cell.

$$C_2 = \left(\frac{U_m}{U_{OC}} - 1\right)\left[\ln\left(1 - \frac{I_m}{I_{SC}}\right)\right]^{-1}. \quad (4)$$

In Equations (2)–(4), $C_1$, and $C_2$ are constants, $I_{SC}$ is the short-circuit current of a photovoltaic cell, $U_{OC}$ is the open-circuit voltage of a photovoltaic cell, $I_m$ is the current at the maximum power point, and $U_m$ is the voltage at the maximum power point.

After simplification, the $I$-$U$ output characteristic model of the photovoltaic cell is obtained, in which the expressions for the constants $C_1$ and $C_2$ are given by Equation (3) and Equation (4), respectively. Under arbitrary environmental conditions, $I_{SC}, U_{OC}, I_m$, and $U_m$ will change according to a certain law. By introducing the corresponding correction coefficient, we can approximately derive the relationship between the solar radiation intensity $G$ and the photovoltaic plate temperature $T$ to these four parameters.

$$I_{SC} = I_{SCref}\frac{G}{G_{ref}}(1 + \alpha\Delta T), \quad (5)$$

$$U_{OC} = U_{OCref}\ln(e + \beta\Delta G)(1 - \gamma\Delta T), \quad (6)$$

$$I_m = I_{mref}\frac{G}{G_{ref}}(1 + \alpha\Delta T), \quad (7)$$

$$U_m = U_{mref}\ln(e + \beta\Delta G)(1 - \gamma\Delta T), \quad (8)$$

$$\Delta T = T - T_{ref}, \quad (9)$$

$$\Delta G = G - G_{ref}. \quad (10)$$

In these equations, $G_{ref} = 1000W/m^2$ is the reference solar radiation intensity under Standard Test Conditions, $T_{ref} = 25^\circ C$ is the reference photovoltaic plate temperature under Standard Test Conditions, $T$ is the actual photovoltaic plate temperature, and $G$ is the actual solar radiation intensity.

The variables $I_{SCref}, U_{OCref}, I_{mref}$, and $U_{mref}$ are the short-circuit current, the open-circuit voltage, and the current and voltage at the maximum power point of the photovoltaic cell under the reference conditions. These are, respectively, the values of the short-circuit current, the open-circuit voltage, and the maximum power point of the photovoltaic cell; $e = 2.781828$ is a natural constant, and $\alpha$, $\beta$, and $\gamma$ are correction coefficients. According to a large amount of relevant experimental data, the typical values recommended for the three correction coefficients are [27]:

$$\alpha = \frac{0.0025}{^\circ C}, \quad \beta = 0.5, \quad \gamma = \frac{0.00288}{^\circ C}. \quad (11)$$

*2.2. Control Equation.* While a car is being driven, the surrounding fluid is air, and for no wind conditions, the air flow speed relative to the car is equal to the speed of the car. It is widely believed that air can be regarded as an incompressible fluid for air flow rates of less than 0.3 times the speed of sound (408 km/h) [28]. The maximum speed considered in this paper is 120 km/h. Therefore, air can be treated as an incompressible fluid here, with constant density. At low speeds, the Reynolds number of the surrounding air is less than the critical Reynolds number, so its flow can be treated as being laminar. When the vehicle is at high speed, the surrounding air Reynolds number is greater than the critical Reynolds number, so it is treated as turbulent flow. The governing equation can be solved by using the continuity equation, the motion equation, and the conservation of energy equation.

For laminar flow, three kinds of conservation equations are introduced, respectively.

The continuous equation:

$$\frac{\partial u_x}{\partial x} + \frac{\partial u_y}{\partial y} + \frac{\partial u_z}{\partial z} = 0. \quad (12)$$

The equation of motion:

$$\frac{\partial \rho u_x}{\partial t} + \frac{\partial(\rho u_x u_x)}{\partial x} + \frac{\partial(\rho u_y u_x)}{\partial y} + \frac{\partial(\rho u_z u_x)}{\partial z} = \rho g_x - \frac{\partial P}{\partial x} + \frac{\partial}{\partial x}\left(\mu\frac{\partial u_x}{\partial x}\right) + \frac{\partial}{\partial y}\left(\mu\frac{\partial u_x}{\partial y}\right) + \frac{\partial}{\partial z}\left(\mu\frac{\partial u_x}{\partial z}\right). \quad (13)$$

$$\frac{\partial \rho u_y}{\partial t} + \frac{\partial(\rho u_x u_y)}{\partial x} + \frac{\partial(\rho u_y u_y)}{\partial y} + \frac{\partial(\rho u_z u_y)}{\partial z} = \rho g_y - \frac{\partial P}{\partial y} + \frac{\partial}{\partial x}\left(\mu\frac{\partial u_y}{\partial x}\right) + \frac{\partial}{\partial y}\left(\mu\frac{\partial u_y}{\partial y}\right) + \frac{\partial}{\partial z}\left(\mu\frac{\partial u_y}{\partial z}\right), \quad (14)$$

$$\frac{\partial \rho u_z}{\partial t} + \frac{\partial(\rho u_x u_z)}{\partial x} + \frac{\partial(\rho u_y u_z)}{\partial y} + \frac{\partial(\rho u_z u_z)}{\partial z} = \rho g_z - \frac{\partial P}{\partial z} + \frac{\partial}{\partial x}\left(\mu\frac{\partial u_z}{\partial x}\right) + \frac{\partial}{\partial y}\left(\mu\frac{\partial u_z}{\partial y}\right) + \frac{\partial}{\partial z}\left(\mu\frac{\partial u_z}{\partial z}\right). \quad (15)$$

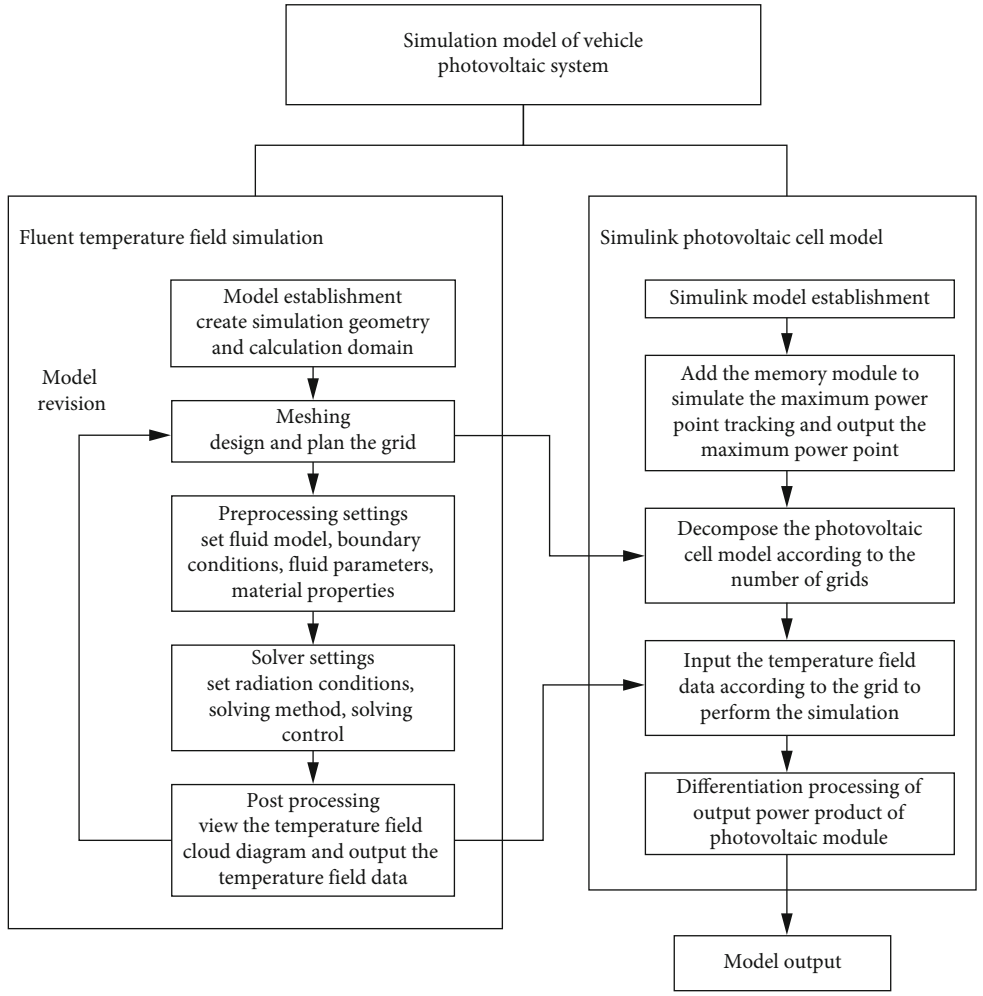


Figure 2: Structure of the simulation model.

Figure 3: Physical diagram of a vehicle photovoltaic system.

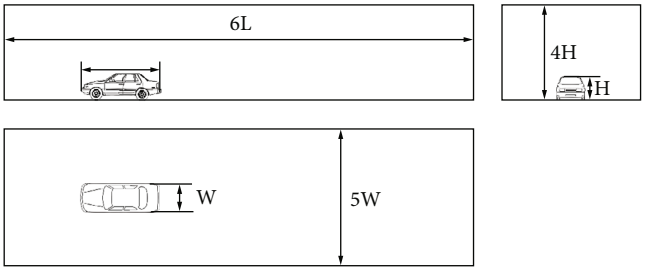


Figure 4: Settings for the calculation domain.

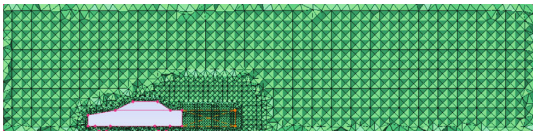

Figure 5: Fluent model grid.

The energy equation:

$$\frac{\partial}{\partial t}(\rho CT) + \frac{\partial}{\partial x}(\rho u_x CT) + \frac{\partial}{\partial y}(\rho u_y CT) + \frac{\partial}{\partial z}(\rho u_z CT) = \frac{\partial}{\partial x}\left(K\frac{\partial T}{\partial x}\right) + \frac{\partial}{\partial y}\left(K\frac{\partial T}{\partial y}\right) + \frac{\partial}{\partial z}\left(K\frac{\partial T}{\partial z}\right) + \frac{\partial P}{\partial t}. \quad (16)$$

In these equations, $u_x, u_y, u_z$ is the velocity vector in the directions of $x$, $y$, and $z$; $g_x, g_y, g_z$ are the acceleration components produced by gravity; $\rho$ is the fluid density; $\mu$ is the aerodynamic viscosity; $P$ is the pressure; $C$ is the specific

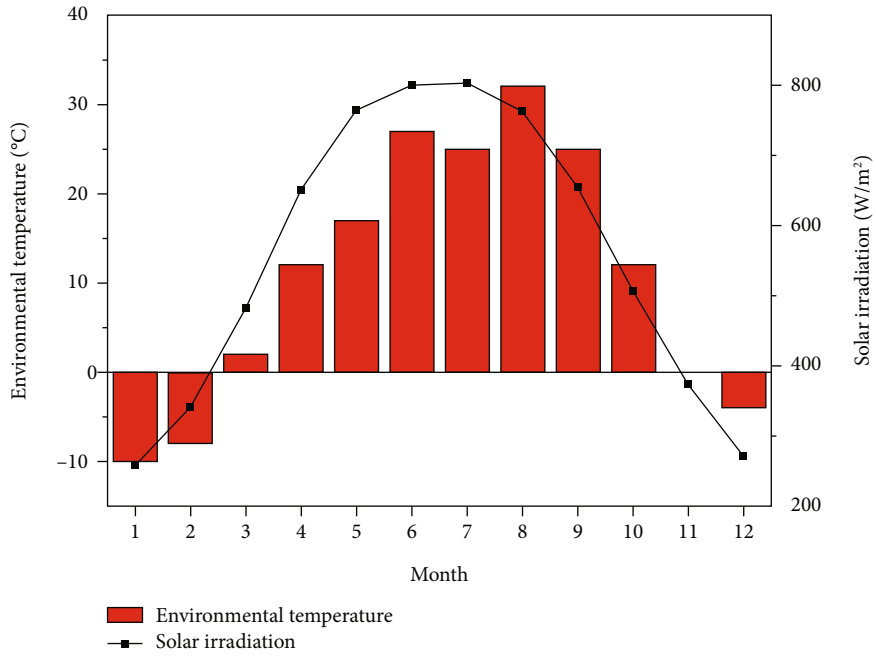


Figure 6: Simulated meteorological data.

heat capacity; $T$ is the temperature; $K$ is the thermal conductivity.

Among the above equations, there are five unknown quantities and five equations, leading to a specific solution.

In the turbulent state, the turbulence model is introduced, and the instantaneous terms of the N-S equations are decomposed into time-averaged terms and wave terms.

The average continuity equation:

$$\frac{\partial \bar{u}_i}{\partial x_i} = 0. \tag{17}$$

The average momentum equation:

$$\rho\left(\frac{\partial \bar{u}_i}{\partial t} + \bar{u}_k \frac{\partial \bar{u}_i}{\partial x_k}\right) = -\frac{\partial \bar{p}}{\partial x_i} + \frac{\partial}{\partial x_j}\left(\mu \frac{\partial \bar{u}_i}{\partial x_j}\right) + \frac{\partial R_{ij}}{\partial x_j}. \tag{18}$$

Of which,

$$R_{ij} = -\rho\overline{u_i' u_j'} = \mu_T\left(\frac{\partial \bar{u}_i}{\partial x_j} + \frac{\partial \bar{u}_j}{\partial x_i}\right) - \frac{2}{3}\mu_T \frac{\partial \bar{u}_k}{\partial x_k}\delta_{ij} - \frac{2}{3}\rho k \delta_{ij}. \tag{19}$$

In the above equations, $\mu$ is the aerodynamic viscosity, $\mu_T$ is the Eddy viscosity coefficient, and $\delta_{ij}$ is the Kronecker function.

To solve the above equations closed-form, it is necessary to determine the value of $\mu_T$. Here we use the 2-equation $RNG\,k-\varepsilon$ model [29], with turbulent kinetic energy equation and turbulent dissipation equation as follows:

$$\rho\frac{\partial k}{\partial t} + \rho \bar{u}_i \frac{\partial k}{\partial x_i} = \frac{\partial}{\partial x_j}\left[\alpha_k(\mu + \mu_T)\frac{\partial k}{\partial x_j}\right] + G_k + G_b - \rho\varepsilon, \tag{20}$$

Table 1: Physical parameters of materials.

| Materials | Physical parameters | Value |
|---|---|---|
| Photovoltaic cell surface (PET) | Density | 1380 $kg/m^3$; |
| | Specific heat capacity | 1400 $J/(kg{\bullet}K)$ |
| | Thermal conductivity | 0.29 $W/(m{\bullet}K)$ |
| Ground (asphalt concrete) | Density | 2460 $kg/m^3$ |
| | Specific heat capacity | 1350 $J/(kg{\bullet}K)$ |
| | Thermal conductivity | 1.08 $W/(m{\bullet}K)$ |
| Body metal | Density | 8030 $kg/m^3$ |
| | Specific heat capacity | 502.48 $J/(kg{\bullet}K)$ |
| | Thermal conductivity | 16.27 $W/(m{\bullet}K)$ |

Table 2: Boundary conditions.

| Boundary | Boundary condition |
|---|---|
| Entrance | Velocity entrance condition |
| Exit | Pressure outlet, 1 standard atmospheric pressure |
| Car body and photovoltaic panel | Fixed nonslip wall |
| Ground | Moving nonslip wall |
| Top and side | Fixed nonslip wall |

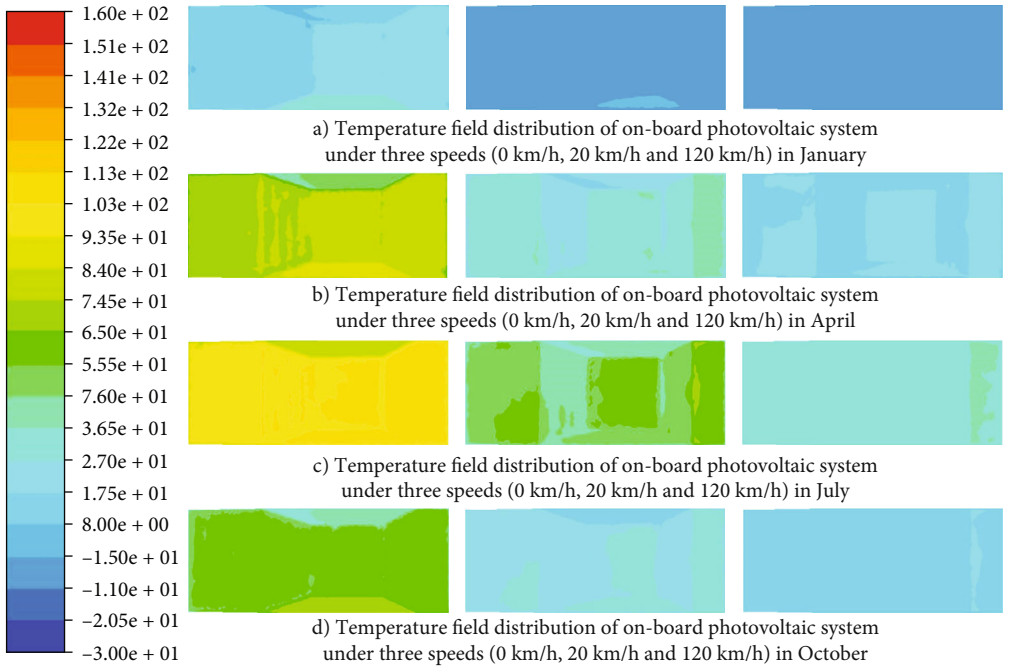


Figure 7: Temperatures of photovoltaic cells at different speeds in 4 months.

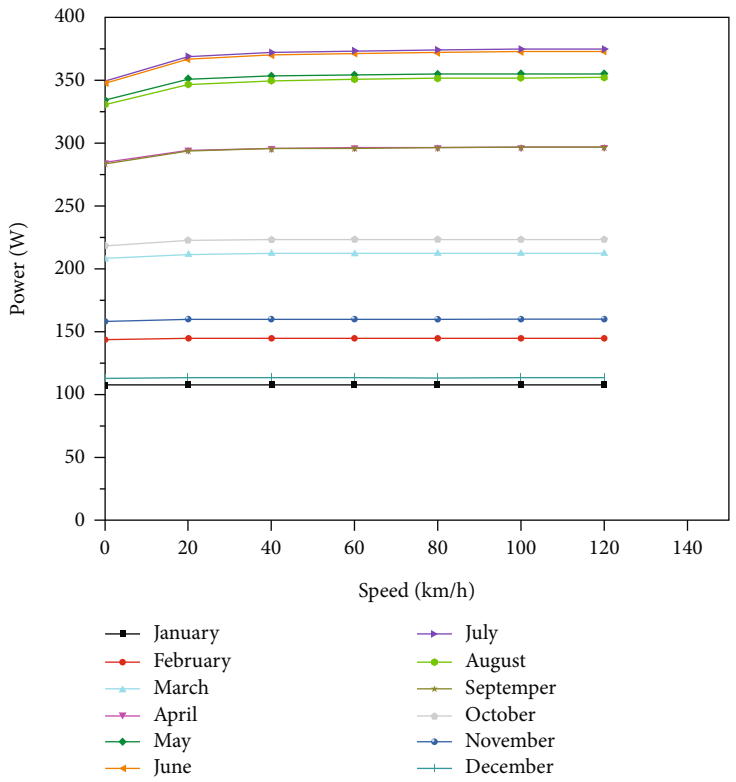


Figure 8: Power-speed images for different months.

Table 3: Correlations for P-v from January to December.

| | Correlation | January Power | February Power | March Power | April Power |
|---|---|---|---|---|---|
| Speed | Correlation coefficient | 0.612 | 0.612 | 0.964 | 1.000 |
| | Sig. (double tail) | 0.144 | 0.144 | 0.000 | 0.000 |
| | Correlation | May Power | June Power | July Power | August Power |
| Speed | Correlation coefficient | 1.000 | 1.000 | 0.964 | 1.000 |
| | Sig. (double tail) | 0.000 | 0.000 | 0.000 | 0.000 |
| | Correlation | September Power | October Power | November Power | December Power |
| Speed | Correlation coefficient | 1.000 | 1.000 | 0.612 | 0.612 |
| | Sig. (double tail) | 0.000 | 0.000 | 0.144 | 0.144 |

$$\rho\frac{\partial\varepsilon}{\partial t}+\rho\bar{u}_i\frac{\partial\varepsilon}{\partial x_i}=\frac{\partial}{\partial x_j}\left[\alpha_\varepsilon(\mu+\mu_T)\frac{\partial\varepsilon}{\partial x_j}\right]+C_{1\varepsilon}\frac{\varepsilon}{k}(G_k+C_{3\varepsilon}G_b)-C_{2\varepsilon}\rho\frac{\varepsilon^2}{k}-R_\varepsilon, \tag{21}$$

Of which,

$$\mu_T=\rho C_\mu\frac{k^2}{\varepsilon}, \tag{22}$$

$$G_k=R_{ij}\frac{\partial\bar{u}_j}{\partial x_j}, \tag{23}$$

$$G_b=-\frac{1}{\rho}\left(\frac{\partial\rho}{\partial T}\right)_p g_i\frac{\mu_T}{Pr_t}\frac{\partial T}{\partial x_i}, \tag{24}$$

$$R_\varepsilon=\frac{C_\mu\rho\eta^3(1-\eta/\eta_0)}{1+\beta_1\eta^3}\frac{\varepsilon^2}{k}. \tag{25}$$

In the above equation, $C_{1\varepsilon}, C_{2\varepsilon}, C_{1\varepsilon}, C_\mu$, and $\eta_0$ are constants; $G_k$ is the turbulent kinetic energy generated by the velocity gradient of laminar flow; $G_b$ is the turbulent kinetic energy generated by buoyancy; and $\alpha_k$ and $\alpha_\varepsilon$ are the turbulent Prandtl numbers for $k$ equation and $\varepsilon$ equation. $Pr_t$ is the turbulent Prandtl number, $\eta = Sk/\varepsilon$, and $S$ is a constant.

After the above equation is manipulated to find a closed from, it is combined with the energy Equation (16), and the temperature can be solved for.

## 3. Simulation Study

*3.1. Simulation Study to Predict Generated Power from Vehicle PV Systems.* The simulation flow chart is shown in Figure 2. When semiflexible photovoltaic cells are installed on a vehicle's surface, they can conform to the vehicle surface and not affect its aerodynamics because of their small thickness and mild deformation, as shown in Figure 3. According to the production principle of photovoltaic cells, equal numbers of photovoltaic units are connected in series and then in parallel, to obtain photovoltaic modules with a certain output voltage, and increased current from the parallel connection of the photovoltaic modules [30]. When the parameters of all the photovoltaic cells are the same, their output current is proportional to the number of photovoltaic cells in parallel ($n_p$), and the output voltage of the photovoltaic cells is proportional to the number of photovoltaic cells in series ($n_s$) [31]. Assuming that the parameters of all the photovoltaic cells are the same, the area of the nonworking area at the edge of the cell is ignored, and the short-circuit current and the maximum power point current can be considered to be proportional to the area of the photovoltaic cell. Based on this relationship, the power prediction model of vehicle photovoltaic system is established. As shown in Figure 2, temperature field data obtained through a Fluent simulation study were extracted, and the Simulink photovoltaic cell model was established at the same time. The photovoltaic module parameters are processed according to the number of grids, and the output power of a single grid area is divided by using for cycle to estimate the actual output power.

Table 4: Fit parameter values.

| | $a$ | $b$ | $c$ | $R^2$ |
|---|---|---|---|---|
| March | 211.0156 | 0.2364 | 4.41E-04 | 0.999 |
| April | 291.1194 | 1.1641 | 3.70E-03 | 0.996 |
| May | 344.2284 | 2.3835 | 1.55E-02 | 0.996 |
| June | 357.0805 | 3.4003 | 6.34E-02 | 0.996 |
| July | 359.0825 | 3.3999 | 5.63E-02 | 0.996 |
| August | 337.9003 | 3.0653 | 9.24E-02 | 0.996 |
| September | 289.0678 | 1.6244 | 3.67E-02 | 0.996 |
| October | 221.2269 | 0.4862 | 2.43E-03 | 0.997 |

*3.2. Fluent Temperature Field Simulation Model.* The type of car modeled in the calculation is a B car, and the three-dimensional model was established using SolidWorks. To simplify the model and improve the calculation efficiency, the creation of complex surfaces such as door handle, exhaust pipes, and rearview mirrors were ignored in the

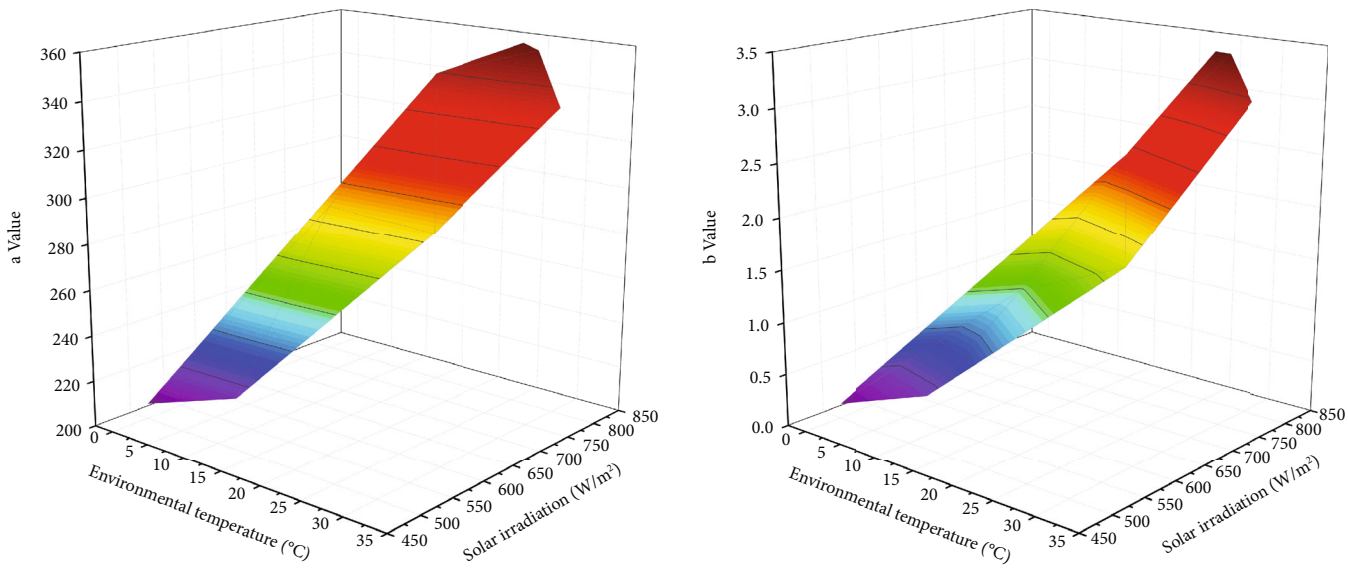


Figure 9: Relationship between parameters $a$, $b$, and $T$, $G$.

modeling process, and the chassis of the automobile model is flattened. The vehicle photovoltaic panel is divided into three parts, which are the engine cover, the roof, and the trunk cover surface. Their shapes and sizes are the same as the car body surface and are represented by sun1 (engine cover), sun2 (roof), and sun3 (trunk cover).

In order to facilitate the analysis and calculation, we need to establish a calculation domain for the model. The calculation domain is a cuboid area around the car model. To fully develop the turbulence, the size of the calculation domain is designed as follows: the entrance distance from the front of the car is equal to its length, the exit distance from the rear is four times the length, the height is four times its height, and the width is five times its width [32]. The three views of the calculation domain are shown in Figure 4.

After a computational domain is established, the entire computing domain is meshed by ICEM CFD (The Integrated Computer Engineering and Manufacturing code for Computational Fluid Dynamics). Because the flow field of the vehicle is more complex and there is a violently turbulent area near the rear of the vehicle, manual intervention is needed in the meshing. The grid near the surface of the vehicle is denser, and the part far away from the car body is sparse. The turbulent area of the rear part is considered carefully to improve the calculation accuracy [33]. The result of the grid is shown in Figure 5.

The factors that need to be considered to simulate the temperature distribution of moving vehicles under natural conditions include solar radiation, atmospheric convection conduction, and ground radiation. To meet the needs of self-defined natural conditions, the DO (discrete ordinates) model was selected for the radiation model. The solar ray tracing model is selected to simulate the geographical location of Changchun City, Jilin Province, China, and typically four sunny and windless days occur every month. The solar radiation intensity and ambient temperature are determined by a query of Chinese meteorological information, and the average value is used for the meteorological condition of that month. The simulated natural conditions are set up, and the simulated meteorological data are shown in Figure 6.

Table 5: Initial fitting parameters for $a$ and $b$.

| | $m$ | $n$ | $p$ | $q$ | $R^2$ |
|---|---|---|---|---|---|
| $a$ | -26.7105 | 0.2947 | 0.4937 | $-8.8371 \times 10^{-4}$ | 0.99 |
| $b$ | -1.5093 | -0.1462 | 0.0038 | $2.6488 \times 10^{-4}$ | 0.98 |

Table 6: Quadratic fitting parameters for $a$ and $b$.

| | $m$ | $n$ | $p$ | $R^2$ |
|---|---|---|---|---|
| $a$ | -18.7278 | -0.2887 | 0.4803 | 0.99 |
| $b$ | -3.9019 | 0.0287 | 0.0786 | 0.93 |

The computational domain includes of multiple boundaries, including the entrance boundary, exit boundary, and wall boundary (body, photovoltaic panel, ground, top, and side). To determine the boundary conditions, the physical properties of the material are determined first. The fluid in the simulation is air, and the solid materials can be divided into three categories: the ground, photovoltaic panel, and body. The specific physical parameters are shown in Table 1.

After determining the physical properties of a material, the boundary conditions for the domain are chosen, as shown in Table 2.

*3.3. Simulink Photovoltaic Cell Model.* According to the mathematical model of photovoltaic cells in Chapter 1.1, the Simulink model was developed, and the photovoltaic cells are modularized according to the number of cells in the Fluent model. The cycle model was introduced to integrate the output of photovoltaic cells in different grids, and the final output is based on the discharge characteristics of photovoltaic cells divided by temperature field.

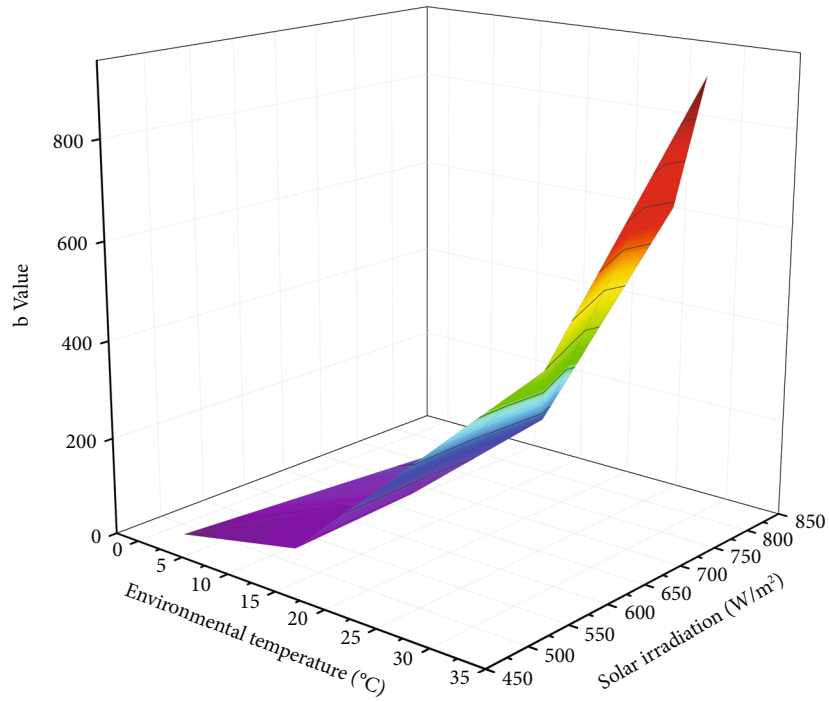


Figure 10: The relationship between the parameter $d$ and parameters $T$ and $G$

## 4. Analysis of Simulation Results

Figure 7 shows the temperature field distribution of photovoltaic cells at speeds of 0 km/h, 20 km/h, and 120 km/h in January, April, July, and October. It can be seen from Figure 7 that the changes in the temperature field in January (winter) are small, and the average temperature is lower. In July (summer), the temperature field changes greatly, and the average temperature is higher. The changes of the temperatures and average temperatures in April (spring) and October (autumn) are in between January and July. This change is mainly related to the solar radiation intensity and also the ambient temperature. These parameters indirectly affect the output characteristics of photovoltaic cells.

Figure 8 shows the relationship between the maximum power of photovoltaic cells and the speed of the vehicle for different months. In the month with higher solar radiation intensity and ambient temperature, compared to the parking/idle state, the maximum power of the photovoltaic cell on the moving vehicle surface obviously increases, and the increasing trend is smaller with the increase of vehicle speed. However, in the month with lower solar radiation intensity and ambient temperature, there is almost no significant difference in the maximum power of photovoltaic cells on the vehicle surface between the parking/idle state and the moving state.

According to the shape of P-v characteristic curve in different months, in the same month, the function of power's change with speed is approximately in the form of $y = a + b \times \ln(x + c)$. There are differences in the curves between different months, so we may consider that there is influence between the solar radiation intensity in different months and the ambient temperature on the parameters $a$, $b$, and $c$.

Table 7: Fitting parameters for the value of $d$.

| | $m$ | $n$ | $p$ | $q$ | $R^2$ |
|---|---|---|---|---|---|
| $d$ | 1.4350 | 1.4350 | $-1.7986 \times 10^{-4}$ | -950.7376 | 0.96 |

Before fitting, the correlation test was carried out on the 12-month P-v data. Because the data are continuous and not approximately a normal distribution, the Spearman correlation analysis method was selected, and SPSS analysis was used to correlate the results of the analysis.

The correlation coefficient is used to characterize how much of the variation in power can be explained by the controlled independent variable speed. The closer correlation coefficient is to 1 indicates the better goodness of fit, and an equation can be considered high confidence when correlation coefficient is greater than 0.95. It can be seen from Table 3 that there is a significant relationship between speed and power in January, February, November, and December with probability greater than 0.95, and there is no correlation between speed and power in these four months. And the significance of speed and power in the other eight months is less than 0.05, the absolute values of correlation coefficients are all greater than 0.96, and the speed and power in these eight months are related. This correlation is strong.

Next, the P-v data for 8 months from March to October are fitted. As shown in Table 4, the variance $R^2$ after fitting is greater than 0.98, and the fitting effect is good.

From the fitted data, we can see that there is an approximately linear relationship between the two parameters $a$ and $b$ and the solar radiation intensity and ambient

temperature. As shown in Figure 9, the model of the relationship between $a$, $b$ and $T, G$ is

$$y = m + nT + pG + qTG \tag{26}$$

After fitting, the specific fitting parameters are shown in Table 5.

Because the order of magnitude of the of $q$ value is much smaller than the value of $m$, $n$, and $p$, to simplify the fitting equation, we make $q = 0$ and repeat the fit process. The fitted parameters are shown in Table 6.

The fit effect is good, as shown by the $R^2$ values in Table 6.

Because the order of magnitude of parameter $c$ is small, the fitting effect is poor, so we magnify $c$. Setting $d = c \times 10^4$, as shown in Figure 10, $d$ has an approximately quadratic relationship with the solar radiation intensity and ambient temperature. The relationship between $d$ and $T, G$ is

$$y = m(T + n)^2 + p(G + q)^2. \tag{27}$$

After fitting, the specific fitted parameters are shown in Table 7.

The fit effect is good.

According to the analysis of mathematical model, the variation of power with speed is similar to the natural log function. Under certain natural conditions, power increases with the increase of speed, but the growth rate of power decreases with increasing speeds. The parameter $a$ as a constant term affects the position of the maximum power point for different conditions. The parameter $b$ affects the growth rate of power and its variation with speed in different months. The parameter $d$ affects the power growth rate of the vehicle from rest to motion.

Figure 11 shows the growth rate of photovoltaic cell power at different speeds for each month. The growth rate for generating power is the highest when the vehicle speed ranges from 0 km/h to 20 km/h. At speeds above 20 km/h, the growth rate of generated power drops and then tends to zero. For the case of the same wind speed changes, the closer it is to summer, the greater the growth rate, and vice versa; in July, the power growth rate is the biggest, and the photovoltaic cell power at 20 km/h speed increases by 5.50% compared with the static motion state. If the vehicle speed increases to 120 km/h, its power increases by 7.33% relative to its static state. The growth rate in December and January is approximately 0. That is, in midwinter the vehicle speed has almost no effect on the output of photovoltaic cells.

In order to study the different growth rates seen in different months, this paper analyzes the relationship between vehicle speed and the rising temperature $\Delta T$ of photovoltaic cell surfaces for natural conditions. Figure 12 shows the $\Delta T$ – v diagram for different months. $\Delta T$ equals $T - T_1$. $T$ is the ambient temperature, and $T_1$ is the working temperature of the photovoltaic cell surface, which is the average temperature in the cloud diagram of the temperature field simulated by Fluent. It can be seen for Figure 12 that in the same month, with the increase of vehicle speed, $\Delta T$ shows a downward trend, and the decline rate decreases gradually. From rest to 20 km/h, $\Delta T$ decreases sharply. At the same speed, the month at higher ambient temperature and more

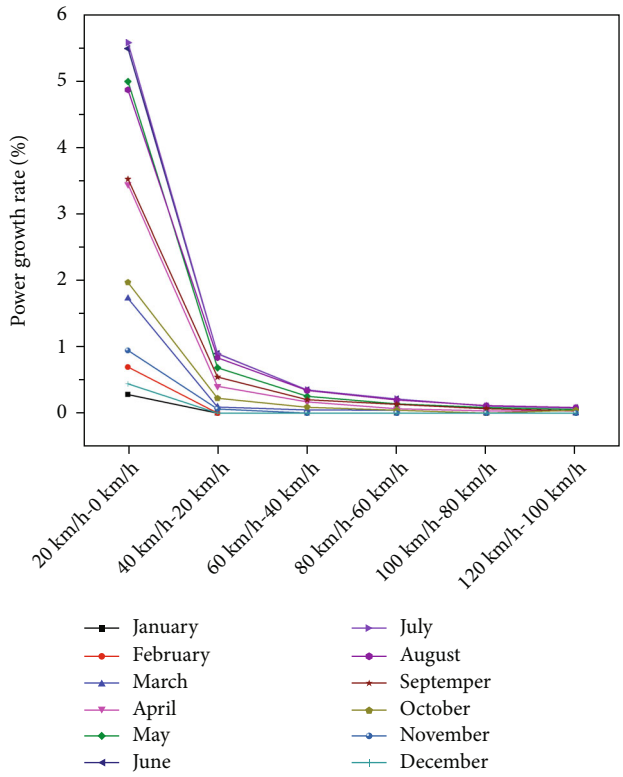


Figure 11: Power growth rate at different speeds in each month

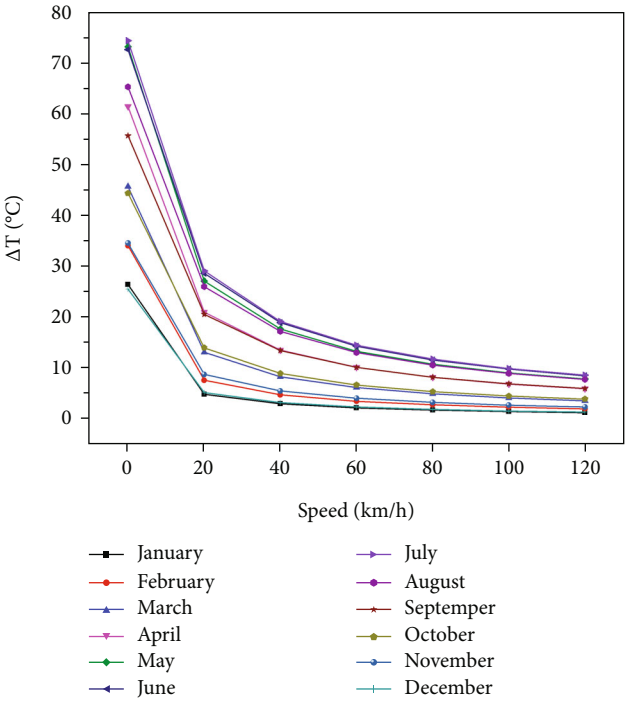


Figure 12: $\Delta T$ – v diagram for different months

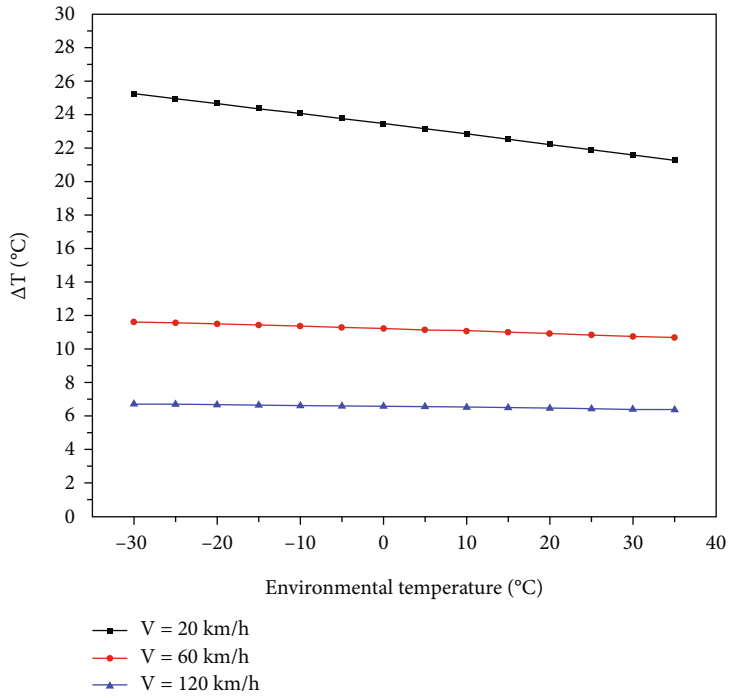


(a) $\Delta T - T$ at $G = 600\ \mathrm{W/m^2}$

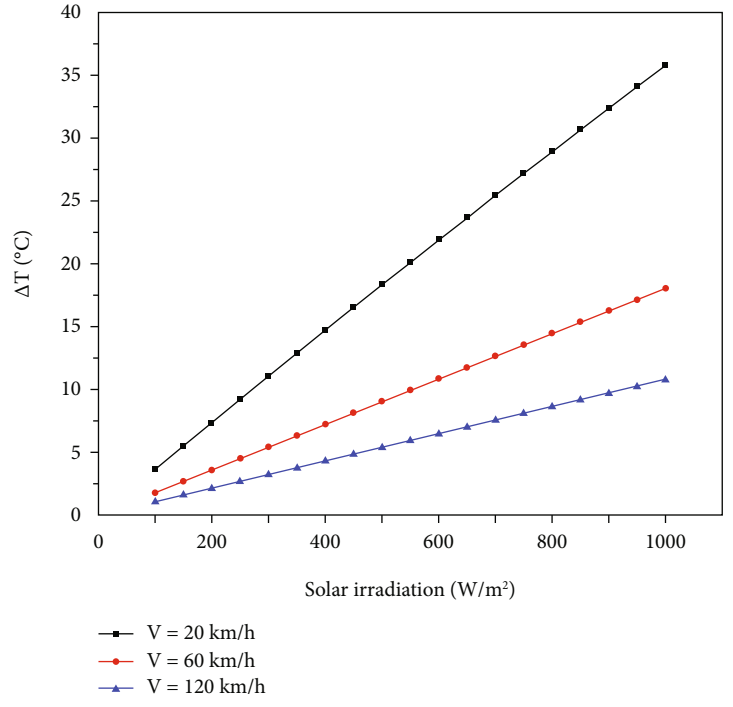


(b) $\Delta T - G$ at $Tamb = 25^{\circ}\mathrm{C}$

Figure 13: Curve for $\Delta T - T$ and $\Delta T - G$.

intense solar radiation will be with greater values of $\Delta T$. From this analysis, it can be seen that in addition to the vehicle speed, the change of $\Delta T$ can be related to the ambient temperature $T$ and solar radiation intensity $G$.

In order to determine other factors that influence of $\Delta T$, we used Fluent to analyze the influence of ambient temperatures $T$ and solar radiation intensity values $G$ on $\Delta T$. For an ambient temperature of 25°C and a solar radiation intensity is 600 $W/m^2$, the relationship diagrams of $\Delta T - G$ and $\Delta T - T$ were obtained when the speed is 20 km/h, 60 km/h, and 120 km/h, as shown in Figure 13. When the ambient temperature is constant, $\Delta T$ increases with increased solar

radiation intensity. This last effect decreases with increasing vehicle speeds. When the solar radiation intensity is constant, ΔT decreases slightly with increased ambient temperatures at low speed (for ambient temperature of 75°C, $\Delta T$ changes by 2-3°C), while $\Delta T$ decreases only slightly with increased ambient temperatures at medium and high speeds. Since the abscissas of the two graphs are not of the same order of magnitude, further function fitting is needed to study the influence of $G$ and $T$ on $\Delta T$.

According to the data for 60 km/h, the ambient temperature is $T$, and the solar radiation intensity is $G$, and $\Delta T$ can be expressed as

$$y = -0.448T^{1.059} + 0.022G^{0.974} + 0.447T^{1.056}G^{-0.0053} + 0.04. \tag{28}$$

$R^2 = 0.96$, showing a good fitting effect.

Analyzing with the model $G^{-0.0053} \approx 1$, when $G$ (solar radiation intensity) is constant, there is a negative correlation between $y$ and $G$, and the effect of $T$ on $y$ is weak. When $T$ (ambient temperature) is constant, there is a positive correlation between $y$ and $G$, and the effect of $G$ on $y$ is strong.

## 5. Conclusions

For this paper, a simulation model for predicting the power generation of vehicle photovoltaic systems was designed. Using the combination of Fluent and Simulink simulations, a photovoltaic cell model is proposed. The influence of vehicle speed on the output power of the vehicle photovoltaic cells for different months in Northeast China is analyzed, to understand the influences of vehicle speed on $\Delta T$, which is the temperature rise of photovoltaic cell surfaces under natural conditions. The influence of solar radiation intensity and ambient temperature on $\Delta T$ at fixed speed is analyzed.

The main conclusions are as follows:

(1) When the ambient temperature and solar radiation intensity are constant, the temperature field of vehicle photovoltaic system decreases with the increase of vehicle speed. The closer to summer, the higher the change rate of temperature field with vehicle speed, and vice versa

(2) The power of the vehicle photovoltaic system in winter is not linked to the vehicle speed. The P-v data curve from March to October is similar to a distorted natural log function, and the output power's rate of change from zero to low speed is greater. With increased vehicle speeds, the power growth rate gradually decreases

(3) In addition to vehicle speed, $\Delta T$ is also affected by solar radiation intensity and ambient temperature, which are positively correlated with solar radiation intensity and negatively correlated with ambient temperatures. Solar radiation intensity is the factor with the most influence

(4) In different months, the effect of vehicle speed on the output power of vehicle photovoltaic system is different. The maximum growth rate of power in summer can reach 7.33%, and the growth rate of power in winter is almost zero. That is to say, the power of vehicle photovoltaic system in Northeast China increases significantly with the increase of vehicle speed in summer, but does not change significantly with the increase of vehicle speed in winter

The predictive model discussed in this paper provides a new solution to the problem of understanding the factors influencing power generation in vehicle photovoltaic systems. It can provide ideas and reference for the research and development of PV-EV system.

## Data Availability

The data presented in this study are available on request from the corresponding author.

## Conflicts of Interest

The authors declare no conflict of interest.

## Acknowledgments

This research was funded by the Youth Program of National Natural Science Foundation of China, grant number 52002143, and by the Monitoring and Early Warning Technology for Truck Loading Status Base on the Analysis of Suspension Vibration Characters, grant number 20190103057JH.

## References

[1] X. Y. Dong, B. Zhang, B. Wang, and Z. H. Wang, "Urban households' purchase intentions for pure electric vehicles under subsidy contexts in China: do cost factors matter?," *Transportation Research Part A: Policy and Practice*, vol. 135, pp. 183–197, 2020.

[2] J. Woo and C. L. Magee, "Forecasting the value of battery electric vehicles compared to internal combustion engine vehicles: the influence of driving range and battery technology," *International Journal of Energy Research*, vol. 44, no. 8, pp. 6483–6501, 2020.

[3] W. Pang, H. W. Yu, Y. Z. Zhang, and H. Yan, "Solar photovoltaic based air cooling system for vehicles," *Renewable Energy*, vol. 130, pp. 25–31, 2019.

[4] D. Kumar, R. K. Nema, and S. Gupta, "A comparative review on power conversion topologies and energy storage system for electric vehicles," *International Journal of Energy Research*, vol. 44, no. 10, pp. 7863–7885, 2020.

[5] Z. Song, Z. G. Ren, Q. L. Deng et al., "General models for estimating daily and monthly mean daily diffuse solar radiation in China's subtropical monsoon climatic zone," *Renewable Energy*, vol. 145, pp. 318–332, 2020.

[6] E. M. Abo-Zahhad, S. Ookawara, A. Radwan, A. H. El-Shazly, M. F. El-Kady, and M. F. C. Esmail, "Performance, limits, and thermal stress analysis of high concentrator multijunction

solar cell under passive cooling conditions," *Applied Thermal Engineering*, vol. 164, p. 114497, 2020.

[7] P. Saxena and N. E. Gorji, "COMSOL simulation of heat distribution in perovskite solar cells: coupled optical-electrical-thermal 3-D analysis," *IEEE Journal of Photovoltaics*, vol. 9, no. 6, pp. 1693–1698, 2019.

[8] O. A. M. Abdelraouf and N. K. Allam, "Towards nanostructured perovskite solar cells with enhanced efficiency: coupled optical and electrical modeling," *Solar Energy*, vol. 137, pp. 364–370, 2016.

[9] N. Dabaghzadeh and M. Eslami, "Temperature distribution in a photovoltaic module at various mounting and wind conditions: a complete CFD modeling," *Journal of Renewable and Sustainable Energy*, vol. 11, no. 5, p. 12, 2019.

[10] S. R. Maadi, M. Khatibi, E. Ebrahimnia-Bajestan, and D. Wood, "Coupled thermal-optical numerical modeling of PV/T module - combining CFD approach and two-band radiation DO model," *Energy Conversion and Management*, vol. 198, article 111781, 2019.

[11] M. Chaabane, W. Charfi, H. Mhiri, and P. Bournot, "Performance evaluation of solar photovoltaic systems," *International Journal of Green Energy*, vol. 16, no. 14, pp. 1295–1303, 2019.

[12] H. Lu and L. Z. Zhang, "Influences of dust deposition on ground-mounted solar photovoltaic arrays: a CFD simulation study," *Renewable Energy*, vol. 135, pp. 21–31, 2019.

[13] B. D. Perovic, D. O. Klimenta, M. D. Jevtic, and M. J. Milovanovic, "A thermal model for open-rack mounted photovoltaic modules based on empirical correlations for natural and forced convection," *Thermal Science*, vol. 23, 6, Part A, pp. 3551–3566, 2019.

[14] S. Zhiqiang and L. Dongyang, "Prediction model of photovoltaic power generation based on time-frequency entropy and neural network," *Journal of Central South University (Natural Science Edition)*, vol. 51, no. 1, pp. 221–230, 2020.

[15] S. Yadir, R. Bendaoud, A. El-Abidi et al., "Evolution of the physical parameters of photovoltaic generators as a function of temperature and irradiance: New method of prediction based on the manufacturer's datasheet," *Energy Conversion and Management*, vol. 203, article 112141, 2020.

[16] C. Kasburg and S. Frizzo, "Deep learning for photovoltaic generation forecast in active solar trackers," *IEEE Latin America Transactions*, vol. 17, no. 12, pp. 2013–2019, 2019.

[17] P. Asef, R. Bargallo, A. E. H. Karci, P. Niknejad, M. R. Barzegaran, and A. C. Lapthorn, "Correlation of solar power prediction considering the nominal operating cell temperature under partial shading effect," *Measurement*, vol. 147, p. 106878, 2019.

[18] S. Issaadi, W. Issaadi, and A. Khireddine, "New intelligent control strategy by robust neural network algorithm for real time detection of an optimized maximum power tracking control in photovoltaic systems," *Energy*, vol. 187, p. 115881, 2019.

[19] A. R. Jatoi, S. R. Samo, and A. Q. Jakhrani, "An improved empirical model for estimation of temperature effect on performance of photovoltaic modules," *International Journal of Photoenergy*, vol. 2019, Article ID 1681353, 16 pages, 2019.

[20] M. Almaktar, H. A. Rahman, M. Y. Hassan, and I. Saeh, "Artificial neural network-based photovoltaic module temperature estimation for tropical climate of Malaysia and its impact on photovoltaic system energy yield," *Progress in Photovoltaics: Research and Applications*, vol. 23, no. 3, pp. 302–318, 2015.

[21] S. Armstrong and W. G. Hurley, "A thermal model for photovoltaic panels under varying atmospheric conditions," *Applied Thermal Engineering*, vol. 30, no. 11-12, pp. 1488–1495, 2010.

[22] H. X. Zang, L. L. Cheng, T. Ding, K. W. Cheung, Z. N. Wei, and G. Q. Sun, "Day-ahead photovoltaic power forecasting approach based on deep convolutional neural networks and meta learning," *International Journal of Electrical Power & Energy Systems*, vol. 118, p. 105790, 2020.

[23] D. S. Tripathy, B. R. Prusty, and K. Bingi, "A k-nearest neighbor-based averaging model for probabilistic PV generation forecasting," *International Journal of Numerical Modelling: Electronic Networks, Devices and Fields*, vol. 35, no. 2, 2022e 2983.

[24] K. G. Ranjan, D. S. Tripathy, B. R. Prusty, and D. Jena, "An improved sliding window prediction-based outlier detection and correction for volatile time-series," *International Journal of Numerical Modelling: Electronic Networks, Devices and Fields*, vol. 34, no. 1, p. e 2816, 2021.

[25] N. G. Bhat, B. R. Prusty, and D. Jena, "Cumulant-based correlated probabilistic load flow considering photovoltaic generation and electric vehicle charging demand," *Frontiers in Energy*, vol. 11, no. 2, pp. 184–196, 2017.

[26] R. Chenni, M. Makhlouf, T. Kerbache, and A. Bouzid, "A detailed modeling method for photovoltaic cells," *Energy*, vol. 32, no. 9, pp. 1724–1730, 2007.

[27] W. De Soto, S. A. Klein, and W. A. Beckman, "Improvement and validation of a model for photovoltaic array performance," *Solar Energy*, vol. 80, no. 1, pp. 78–88, 2006.

[28] W. Qin, S. Houhuan, and W. Congbiao, "Numerical simulation and analysis of car outflow field," *Mechanical Science and Technology*, vol. 34, no. 5, pp. 780–784, 2015.

[29] V. K. Krastev, A. d'Adamo, F. Berni, and S. Fontanesi, "Validation of a zonal hybrid URANS/LES turbulence modeling method for multi-cycle engine flow simulation," *International Journal of Engine Research*, vol. 21, no. 4, pp. 632–648, 2020.

[30] V. Panchenko, A. Izmailov, V. Kharchenko, and Y. Lobachevskiy, "Photovoltaic solar modules of different types and designs for energy supply," *International Journal of Energy Optimization and Engineering*, vol. 9, no. 2, pp. 74–94, 2020.

[31] W. Zhuoling and L. Xiaoying, "Research on mathematical model of photovoltaic array based on Matlab," *Industrial and Mining Automation*, vol. 37, no. 12, pp. 40–43, 2011.

[32] R. M. Janicki and A. Piechna, "Examining influence of a rooftop cargo carrier position on automobile aerodynamics," in *Computational Technologies In Engineering. Vol. 2078*, Melville: Amer Inst Physics, 2019.

[33] T. Janson and J. Piechna, "Numerical analysis of Aerodynamic characteristics of a of high-speed car with movable bodywork elements," *Archive of Mechanical Engineering*, vol. 62, no. 4, pp. 451–476, 2015.